

MOX-Report No. 18/2022

**An image-based computational fluid dynamics study of
mitral regurgitation in presence of prolapse**

Bennati, L; Vergara, C; Giambruno, V; Fumagalli, I; Corno,
A.F; Quarteroni, A; Puppini, G; Luciani, G.B

MOX, Dipartimento di Matematica
Politecnico di Milano, Via Bonardi 9 - 20133 Milano (Italy)

mox-dmat@polimi.it

<http://mox.polimi.it>

An image-based computational fluid dynamics study of mitral regurgitation in presence of prolapse

Bennati, L¹; Vergara, C²; Giambruno, V³; Fumagalli, I⁴; Corno, A.F⁵;
Quarteroni, A^{4,6}; Puppini, G⁷; Luciani, G.B³

April 8, 2022

¹ Department of Surgery, Dentistry, Pediatrics, and Obstetrics/Gynecology, University
of Verona, O. C. M. Piazzale Stefani 1, Verona, 37126, Italy

`lorenzo.bennati@univr.it`

² 2LaBS, Dipartimento di Chimica, Materiali e Ingegneria Chimica “Giulio Natta”,
Politecnico di Milano, Piazza Leonardo da Vinci 32, Milan, 20133, Italy.

`christian.vergara@polimi.it`

³ Division of Cardiac Surgery, Department of Surgery, Dentistry, Pediatrics, and
Obstetrics/Gynecology, University of Verona, O. C. M. Piazzale Stefani 1, Verona,
37126, Italy.

`vincenzo.giambruno@aovr.veneto.it`, `giovanni.luciani@univr.it`

⁴ MOX, Dipartimento di Matematica, Politecnico di Milano, Piazza Leonardo da Vinci
32, Milan, 20133, Italy.

`ivan.fumagalli,alfio.quarteroni@polimi.it`

⁵ Children’s Heart Institute, UT Health, McGovern Medical School, 6431 Fannin
Street, Houston, Texas, 77030, USA.

`antonio.f.corno@uth.tmc.edu`

⁶ Ecole Polytechnique Federale de Lausanne, Rte Cantonale, Lausanne, 1015,
Switzerland.

⁷ Department of Radiology, University of Verona, O. C. M. Piazzale Stefani 1, Verona,
37126, Italy.

`giovanni.puppini@aovr.veneto.it`

Keywords: Mitral valve regurgitation, Image-based computational fluid dy-
namics, Wall shear stresses, Cine-MRI images

Abstract

Purpose: In this work we performed an imaged-based computational
study of the systolic fluid dynamics in presence of Mitral Valve Regurgi-
tation (MVR). In particular, we compare healthy and different regurgitant
scenarios with the aim of quantifying different hemodynamic quantities.

Methods: We performed computational fluid dynamic (CFD) simu-
lations in the left ventricle, left atrium and aortic root, with a resistive
immersed method, a turbulence model, and with imposed systolic wall mo-
tion reconstructed from Cine-MRI images, which allowed us to segment also

the mitral valve. For the regurgitant scenarios we considered an increase of the heart rate and a dilation of the left ventricle.

Results: Our results highlighted that MVR gave rise to *regurgitant jets* through the mitral orifice impinging against the atrial walls and scratching against the mitral valve leading to high values of Wall Shear Stresses (WSS) with respect to the healthy case.

Conclusion: CFD with prescribed wall motion and immersed mitral valve revealed to be an effective tool to quantitatively describe hemodynamics in the case of MVR and to compare different regurgitant scenarios. Our findings highlighted in particular the presence of transition to turbulence in the atrium and allowed us to quantify some important cardiac indices such as cardiac output and WSS.

1 Introduction

Mitral Valve Regurgitation (MVR) is a congenital or acquired pathological condition of the mitral valve leading to an incomplete closure of the leaflets during the systolic phase, causing a retrograde blood flow from the left ventricle to the left atrium. The major complications are atrial fibrillation or flutter, pulmonary arterial hypertension and heart failure [1]. Epidemiological studies estimated that MVR occurs in up to 10% of the worldwide population [2].

The quantitative assessment of blood dynamics quantities, such as pressure, velocity and stresses, in the presence of MVR during the systolic phase is crucial for the understanding of the phenomena and to elaborate the diagnosis. For example, the regurgitant volume (RV) and the regurgitant fraction (RF) [3] can help physicians in assessing the severity of the pathological condition and potentially helping the design of treatments [4, 5].

Computational methods in realistic cardiac geometries represent a non invasive way to provide blood dynamics information and help the surgeons [6, 7, 8]. Computational studies investigating the mitral valve and its interaction with the blood flow have been proposed since the early 2000's, and can be divided into two categories: i) Fluid-Structure Interaction (FSI) models and ii) Computational Fluid Dynamics (CFD) models with imposed wall motion.

Regarding the FSI approach, some authors investigated the mitral valve dynamics in physiological conditions [9, 10, 11, 12, 13], in the case of calcific leaflets [9], to model surgical interventions as the neochordae replacement [14], and to account for MVR [15, 16]. In [15], MVR has been modeled by means of an idealized diode whilst in [16] the healthy configuration has been deformed.

In order to reduce the high computational costs of FSI simulations, CFD models with imposed ventricular and leaflets motion provided by dynamic imaging have also been considered. Such models require a huge effort in elaborating the dynamic images and in merging them with CFD. However, they noticeably simplify the problem from the modeling point of view. The majority of such works are based on images provided by ultrasound (US) techniques (like 3D

echocardiography). 3D Echo has the advantage of providing high temporal resolution, particularly useful when resolving the rapid movements of the mitral valve leaflets [6]. For example, in [17, 18] the authors prescribed both the ventricle and the mitral valve motion to study the ventricular flow in physiological conditions. In [19], the authors reconstructed the ventricle size and shape from Computer Tomography (CT) scans and the mitral valve from US to predict the outcomes of the mitral clip, a surgical technique used to restore the mitral valve function. In [20] the effects of the chordae tendineae on the systolic flow was investigated, by reconstructing both the ventricle and the mitral valve.

Another dynamic imaging technique used for ventricular CFD is cine-MRI. However, such technique has been used to reconstruct only the motion of the ventricle whereas a different modeling of the mitral valve has been considered. For example, we cite [21] where the authors investigated the effect of incorporating an idealized mitral valve in patients affected by pulmonary artery hypertension, and [8, 22] where a template of mitral valve was included to study the systolic anterior motion and the hypertrophic cardiomyopathy.

Regarding the study of the MVR by CFD with imposed motion, we cite [23], where the authors tested and compared different types of mitral valve prolapse from US images.

This work aims at providing an original study of the systolic blood dynamics in the left ventricle in physiological and MVR conditions. For this purpose, we introduced some novelties in the context of computational models for ventricular fluid-dynamics. First, we adapted to the systolic phase (closed mitral valve) a method based on radial sampling cine-MRI acquisitions (see [24] for the case of structural analyses). Second, we applied such reconstruction in the context of a systolic CFD with ventricular motion, prescribed by another (not radial) cine-MRI acquisition. The third novelty of the paper consisted in the comparison of the systolic blood dynamics in physiological and MVR conditions, where for the latter case we considered two scenarios, i.e. an increment of the heart rate and a ventricular dilation [25].

2 Materials and Methods

2.1 Description of the scenarios

In this work we provided a comparison of blood flow dynamics in scenarios with healthy and regurgitant mitral valves during the systolic phase¹. To do this, we considered the same geometric and moving conditions for the left ventricle, for the aorta, and for the left atrium. In this respect, we created three different virtual scenarios:

¹Notice that for the regurgitant cases R1 and R2 (see below) we also considered the isovolumic contraction when both the valves are closed, see Sect. 3.4

- *healthy* (H): we inserted a structurally normal mitral valve (taken from dedicated MRI images) and we considered a heart rate equal to 75 bpm/min (duration of the systolic phase $T_S = 0.32$ s);
- *regurgitant with increased heart rate* (R1): we inserted a regurgitant mitral valve with a prolapse of the posterior leaflet (taken from dedicated MRI images) and we increased the basal heart rate to 90 bpm/min ($T_S = 0.26$ s [26, 27]);
- *regurgitant with dilatation* (R2): we inserted the same regurgitant mitral valve of R1, with heart rate equal to 75 bpm/min, and we dilated all the geometry (ventricle, atrium, aorta).

These scenarios represent different stages of the pathological evolution of the heart function in the case of MVR due to prolapse leading to a decrease of the cardiac output. To compensate, in an *early stage* the heart rate spontaneously increases (R1) [25]. However, this leads to a reduction of the duration of the diastolic phase, making the coronary arteries perfusion less effective over the time. Thus, in a *medium-long term*, the early compensatory changes are gradually replaced by a remodeling process with dilation of the left ventricle and restoring of the basal heart rate (R2). The resultant increase of the stroke volume tends to compensate for the low cardiac output [25].

3 Materials and Methods

3.1 Description of the scenarios

In this work we provided a comparison of blood flow dynamics in scenarios with healthy and regurgitant mitral valves during the systolic phase². To do this, we considered the same geometric and moving conditions for the left ventricle, for the aorta, and for the left atrium. In this respect, we created three different virtual scenarios:

- *healthy* (H): we inserted a structurally normal mitral valve (taken from dedicated MRI images) and we considered a heart rate equal to 75 bpm/min (duration of the systolic phase $T_S = 0.32$ s);
- *regurgitant with increased heart rate* (R1): we inserted a regurgitant mitral valve with a prolapse of the posterior leaflet (taken from dedicated MRI images) and we increased the basal heart rate to 90 bpm/min ($T_S = 0.26$ s [26, 27]);

²Notice that for the regurgitant cases R1 and R2 (see below) we also considered the isovolumic contraction when both the valves are closed, see Sect. 3.4

- *regurgitant with dilatation* (R2): we inserted the same regurgitant mitral valve of R1, with heart rate equal to 75 bpm/min, and we dilated all the geometry (ventricle, atrium, aorta).

These scenarios represent different stages of the pathological evolution of the heart function in the case of MVR due to prolapse leading to a decrease of the cardiac output. To compensate, in an *early stage* the heart rate spontaneously increases (R1) [25]. However, this leads to a reduction of the duration of the diastolic phase, making the coronary arteries perfusion less effective over the time. Thus, in a *medium-long term*, the early compensatory changes are gradually replaced by a remodeling process with dilation of the left ventricle and restoring of the basal heart rate (R2). The resultant increase of the stroke volume tends to compensate for the low cardiac output [25].

3.2 Acquisition of cine-MRI images

Cardiac cine-MRI data were provided by the Department of Radiology of Borgo Trento Hospital, Verona, Italy. Ethical review board approval and informed consent were obtained from all patients.

The acquisitions were performed with the Achieva 1.5T (TX) - DS (Philips, Amsterdam, Netherlands) technology with the following characteristics:

- *Left ventricle*: i) volumetric short-axis series made of 15 slices with thickness and distancing of 8 mm along the left ventricle main axis, with a spatial resolution of 1 mm; ii) a set of single-slices, two-dimensional long-axis acquisitions on the so-called two-chambers and four-chambers planes, with space resolution of 1 mm and slice thickness of 8 mm. Both series had a time resolution equal to 30 frames/cardiac cycle. This protocol was carried out for a subject who did not present any alteration of the left ventricle wall and movement;
- *Mitral valves*: two-dimensional long-axis series of 18 evenly rotated (one every 10) planes around the axis passing through the annular center and aligned with the left ventricle. Time resolution equals to 30 frames/cardiac cycle, spatial resolution equals to 1.25 mm, and slice thickness to 8 mm. This protocol was repeated for a healthy patient and one with a regurgitant mitral valve.

In what follows we describe how such images were elaborated and reconstructed.

3.3 Geometric reconstruction of the left ventricular endocardium

In this section we described the strategy followed to reconstruct the geometry and the displacement field of the left ventricular endocardium.

The starting point were the volumetric short-axis images, which are *ad hoc* series for the reconstruction of the left ventricular anatomy. However, one of the main disadvantages often characterizing such images in the daily clinical practice is the low resolution among slices (in our case about 8mm). As a consequence it is difficult to capture some important findings of the heart contraction, as the longitudinal shortening of the ventricle. To account for this, in this work we applied the Short-Long Axis Merging (SLAM) algorithm, proposed in [22], which consists in enhancing the short-axis images by merging them with long-axis acquisitions (2 and 4 chambers views). This allowed us to obtain enhanced time-dependent series of volumetric images with a uniform space resolution of 1 mm in all directions.

Starting from these enhanced images, we segmented and reconstructed the shape of the endocardium and epicardium at six instants from the end diastolic (ED) to the end systolic (ES) configuration, by adopting the semi-manual segmentation algorithm proposed in [28] and implemented in the Medical Image Toolkit (MITK) open-source software (www.mitk.org) [29, 30]. This allowed us to extract the region of the endocardium from the apex to the level of the valvular ring, by using the Vascular Modeling Toolkit (VMTK) (www.vmtk.org) [31] and suitable tools for cardiac mesh generation [32].

These steps were repeated for all the six frames, obtaining surface meshes made of triangles, representing the configurations of the endocardium during its contraction phase. Then, we registered the displacement needed to pass from a configuration to another one by exploiting the non-affine B-splines algorithm implemented in the Elastix open source library (<http://elastix.isi.uu.nl>) [33]. This allowed us to compute the displacement fields (with respect to the ES configuration) at the six different time instants.

3.4 Inclusion of left atrium, aortic valve, and aorta

We completed the ventricular geometry by adding left atrium, aortic root and aortic valve. The strategy adopted is showed in Figure 1.

Since the ventricular cine-MRI images at disposal were not sufficient to allow a 3D reconstruction of the left atrium, aorta and aortic valve, that are only partially visible in long-axis images, we considered the *Zygote* template geometry of the internal atrial surface and the aortic valve (<https://www.zygote.com>). In particular, we merged such templates at the ES configuration to the reconstructed ventricular endocardium. For the healthy case H, we started our simulation at the aortic valve opening instant t_0 since we could not simulate the isovolumic phase due to blood incompressibility. However, we observed that for the regurgitant cases R1 and R2 the ventricular pressure at t_0 is lower than the aortic one due to mitral regurgitation, which retarded the aortic valve opening. Thus, it was mandatory in such cases to start our simulations from the close configuration for both the valves. Moreover, we generated an aortic flow extension of the left ventricle outflow tract to account for the aorta (steps A and B in

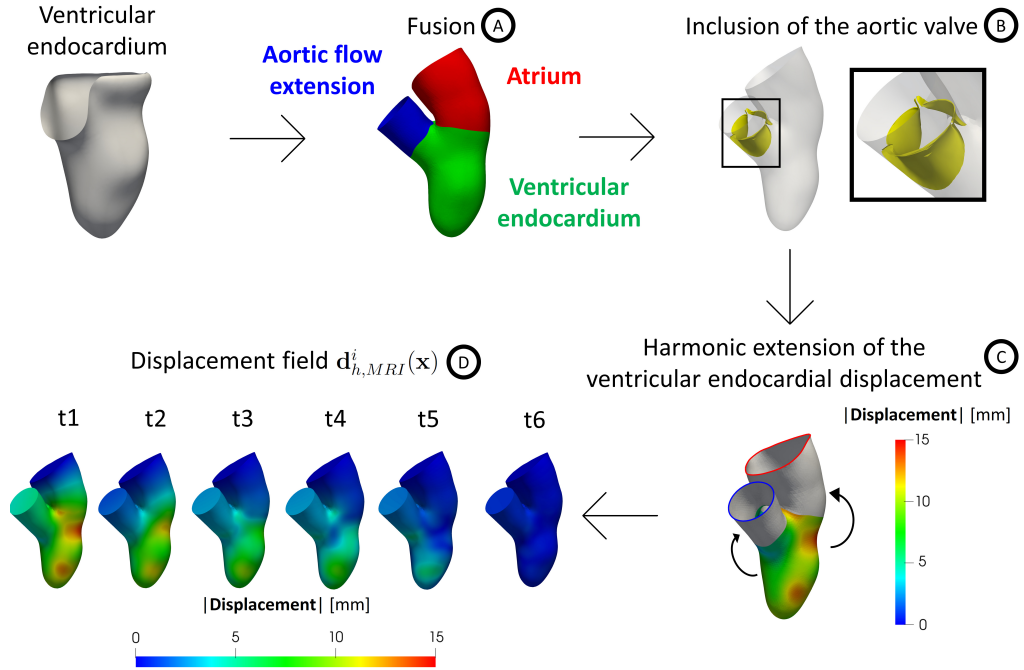


Figure 1: Steps to complete the geometry and its displacement. A: union of the atrium with the ventricular endocardium and addition of an aortic flow extension. B: inclusion of a template of the aortic valve (as an example, here we reported the open configuration). C: harmonic extension of the ventricular endocardial displacement for the atrium and for the aorta. D: magnitude of the displacement field $\mathbf{d}_{h,MRI}^i(\mathbf{x})$ at the six time instants with respect to the ES configuration.

Fig 1). These operations were done by using suitable algorithms in VMTK [32]. This allowed us to obtain a surface mesh of the complete geometry (ventricular endocardium, left atrium and aorta) at the ES configuration.

Then, to provide a displacement field also to the atrium and the aortic root, we harmonically extended the ventricular endocardial displacement to the corresponding surfaces (step C in Fig 1). In such a way, a displacement field was defined for each point of the complete mesh at each of the six frames. After, we performed a L^2 projection of such data on the computational mesh used to perform Finite Elements simulations (see next section) to obtain the functions $\mathbf{d}_{h,MRI}^i(\mathbf{x})$, $i = 1, \dots, 6$, (see Step D in Figure 1 where we reported the magnitude of $\mathbf{d}_{h,MRI}^i(\mathbf{x})$ at the six time instants). Notice that the first instant (t1) refers to the ED configuration, whereas the last one (t6) to the ES configuration.

3.5 Geometric reconstruction of the mitral valve

In this section we reported the steps followed to reconstruct the two mitral valves at disposal in the systolic configuration and to build the three virtual scenarios under study (See Sect. 3.1).

For the reconstruction of the mitral valves, we adapted to the systolic phase the method proposed in [24] for the diastolic case, see Figure 2. The starting point are cine-MRI images of a healthy and of a regurgitant mitral valve acquired based on a protocol proposed for the first time in [24]. The operator performed a radial sampling by using 18 planes rotated every 10° around the axis passing through the center of the annular plane and aligned with the left ventricle apex. The result of this protocol is reported in step A in Fig 2 and represents the input data to reconstruct the mitral valve.

Then, such mitral images were imported in 3D Slicer (<https://slicer.org/>) and for each of the 18 acquired longitudinal planes we traced the leaflets profile in the ED configuration by using a spline curve sampled in 32 points (step B in Fig 2). We repeated this operation for all the 18 planes to obtain the final 3D point cloud representing the mitral valve profile (step C in Fig 2). These data are stored in a matrix of cloud points composed by 1152 rows (32 sampling points \times 36 leaflets profiles) \times 3 columns (x, y and z coordinate). After, we imported this matrix in Matlab (www.mathworks.com) to perform a smoothing process in order to reduce possible inaccuracies due to image noise and to the manual segmentation of the leaflets. To do this, we created a new matrix where blocks of 36 consecutive rows represent the (36) points of a ring (32 rings in total), with the first ring corresponding to the annulus and the last one to the free margin. Then, the points of each ring were fitted by using a B-Spline (see step D in Fig 2). This resulted in a new 3D point cloud of 32000 rows (1000 points \times 32 rings) \times 3 columns (x, y and z coordinate), see step E in Fig 2. Then, for each of the two mitral valves, a surface mesh with a uniform edge length was obtained from the 3D point cloud using MeshMixer (<https://www.meshmixer.com>), see step F in Fig 2.

Finally, the mitral valves were added to the reconstructed geometry (Fig 1) to build the three virtual scenarios under study (step G in Fig 2). We point out that geometry and displacement field $\mathbf{d}_{h,MRI}^i(\mathbf{x})$ of H and R1 are the same at each of the six time instants. Instead, to obtain the configuration of R2, we dilated the geometry of R1 to reach a diameter of the left ventricle cavity equal to 7.2 cm; this value represents the maximum diameter of a dilated left ventricle cavity in presence of MVR according to [34, 35]. In particular, we expanded at each time frame the R1 geometry and the displacement field $\mathbf{d}_{h,MRI}^i(\mathbf{x})$ by a factor of 1.25.

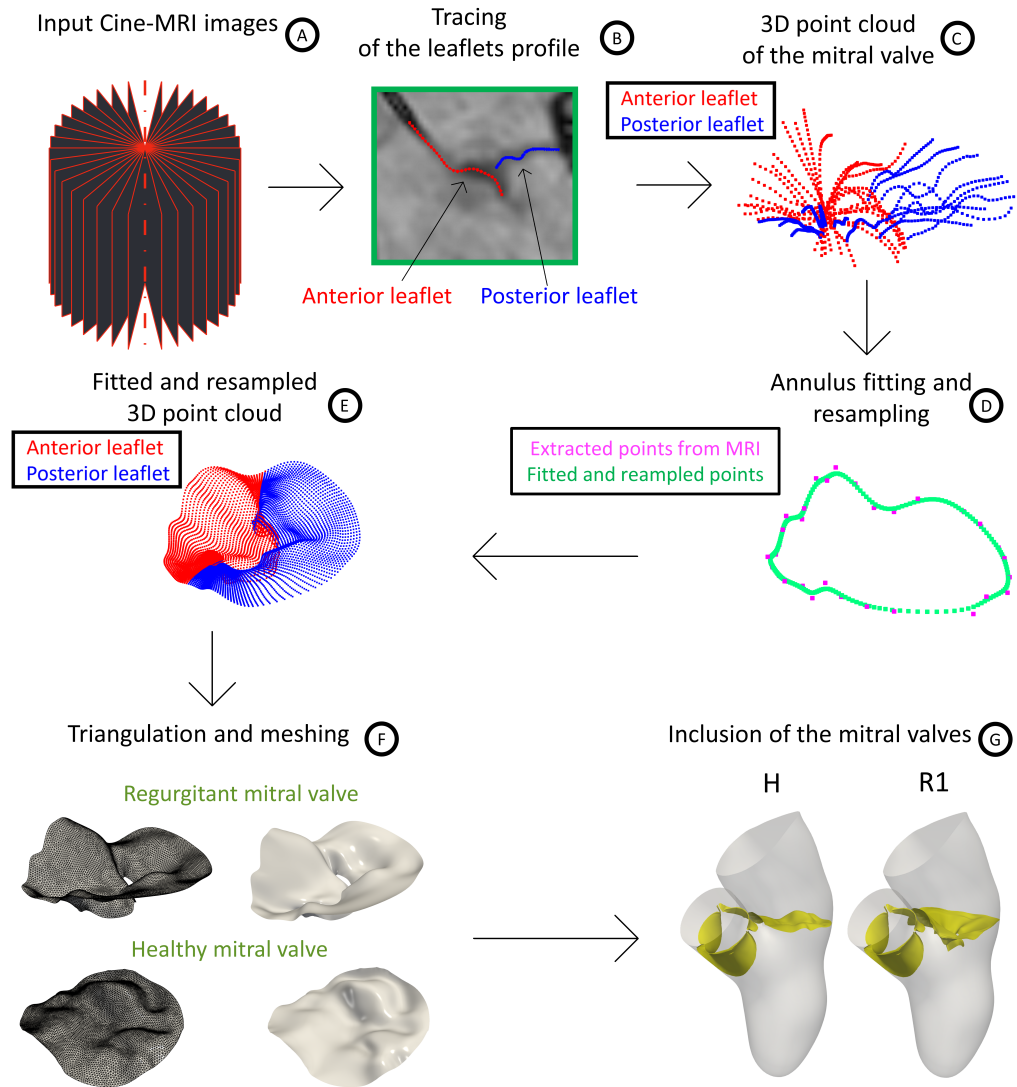


Figure 2: Flow chart to reconstruct the mitral valves and to define the virtual scenarios. A: cine-MRI images of the mitral valve. B: tracing of the leaflets profile on each of the 18 longitudinal planes. C: 3D point cloud of the mitral valve obtained by tracing the leaflets profiles in all the planes. D: fitting and resampling procedure of the rings (the case of the annulus is reported here as an example). E: the 3D point cloud as a result of the fitting and resampling procedure performed for all the rings. F: creation of a surface mesh of the mitral valve. G: generation of scenarios H and R1 (to obtain scenario R2, we dilated the geometry and the displacement field of R1 by a factor 1.25).

3.6 Mathematical and numerical modeling

Let $\Omega(t)$ be the computational moving domain of the complete geometry. The boundaries of $\Omega(t)$ are displayed in Figure 3, left.

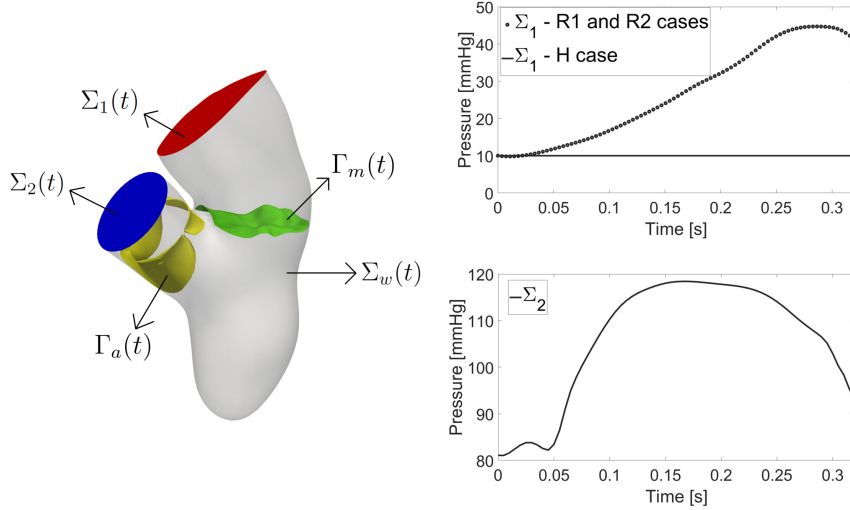


Figure 3: Left: computational domain $\Omega(t)$ with its boundaries: $\Sigma_w(t)$ represents the ventricular endocardium and the physical wall of the atrium and aortic root; $\Sigma_1(t)$ is the atrium outlet and $\Sigma_2(t)$ the aortic outlet. $\Gamma_a(t)$ is the surface of the aortic valve and $\Gamma_m(t)$ the surface of the mitral valve. Right: trend in time of the pressure imposed at the outlets $\Sigma_1(t)$ (up) and $\Sigma_2(t)$ (bottom) (for R1 the frequency has been suitably adapted).

The motion of Ω is determined by the displacement field $\mathbf{d}_{h,MRI}^i(\mathbf{x})$ reconstructed and showed in Figure 1. However, $\mathbf{d}_{h,MRI}^i(\mathbf{x})$ has been obtained only at the MRI acquisition times ($i = 1, \dots, 6$) and thus we employed a spline interpolation to obtain $\mathbf{d}_{h,MRI}(\mathbf{x}, t)$ for all $t \in [0, T_S]$.

We considered blood as an incompressible Newtonian fluid with density $\rho = 1.06 \cdot 10^3 \text{ kg/m}^3$ and dynamic viscosity $\mu = 3.5 \cdot 10^{-3} \text{ Pa} \cdot \text{s}$. The systolic contraction of the complete geometry is taken into account by solving the fluid problem in an Arbitrary Lagrangian–Eulerian (ALE) formulation [36, 37]. The fluid domain is obtained by starting from the ventricular displacement $\mathbf{d}_{h,MRI}$ and by extending it into Ω through the solution of a linear elastic problem [38].

The presence of the valves is accounted by a resistive immersed method inspired by the one proposed in [39, 40]. In particular, we used the Resistive Immersed Implicit Surface (RIIS) method [41], whose main advantage is that the computational mesh and the surface of the valve do not need to be conforming.

To capture the transition to turbulence, we used the Large Eddy Simulation (LES) σ -model proposed for ventricular blood dynamics in [42] and successfully used in different hemodynamic applications [43, 44, 45].

In this framework, let index n indicate the approximation of quantities at time $t^n = n\Delta t$, where Δt is the time discretization parameter. Then, with a first-order semi-implicit time discretization, the problem at time step t^{n+1} reads:

1) Solve a linear elasticity problem to find the displacement $\widehat{\mathbf{d}}^{n+1}$ of the fluid domain³:

$$\begin{cases} -\nabla \cdot \left[2\mu_{EXT}\nabla^s \widehat{\mathbf{d}}^{n+1} + \lambda_{EXT} \left(\nabla \cdot \widehat{\mathbf{d}}^{n+1} \right) \mathbf{I} \right] = \mathbf{0} & \text{in } \widehat{\Omega}, \\ \widehat{\mathbf{d}}^{n+1} = \widehat{\mathbf{d}}_{h,MRI}^{n+1} & \text{on } \widehat{\Sigma}_w, \\ \widehat{\mathbf{d}}^{n+1} = \mathbf{0} & \text{on } \widehat{\Sigma}_1, \\ \left[2\mu_{EXT}\nabla^s \widehat{\mathbf{d}}^{n+1} + \lambda_{EXT} \left(\nabla \cdot \widehat{\mathbf{d}}^{n+1} \right) \mathbf{I} \right] \cdot \widehat{\mathbf{n}} = \mathbf{0} & \text{on } \widehat{\Sigma}_2, \end{cases} \quad (1)$$

with ∇^s the symmetric gradient and \mathbf{I} the identity matrix. μ_{EXT} and λ_{EXT} were both set to the value of 0.4 Pa to avoid mesh elements degeneration during the deformation. Notice the homogeneous Dirichlet condition on Σ_1 , since we want to keep fixed the atrial section, and the homogeneous Neumann condition on Σ_2 in order to let it free to move in accordance with the rest of the geometry.

2) Update the fluid domain $\Omega^{n+1} = \widehat{\Omega} + \widehat{\mathbf{d}}^{n+1}$ and calculate the fluid domain velocity $\widehat{\mathbf{u}}_{ALE}^{n+1} = (\widehat{\mathbf{d}}^{n+1} - \widehat{\mathbf{d}}^n)/\Delta t$;

3) Compute the wall velocity $\widehat{\mathbf{u}}_{h,MRI}^{n+1} = (\widehat{\mathbf{d}}_{h,MRI}^{n+1} - \widehat{\mathbf{d}}_{h,MRI}^n)/\Delta t$;

4) Solve the ALE Navier-Stokes equations in the known domain Ω^{n+1} to find the pressure p^{n+1} and the blood velocity \mathbf{u}^{n+1} :

$$\begin{cases} \rho \frac{\mathbf{u}^{n+1} - \mathbf{u}^n}{\Delta t} + \rho (\mathbf{u}^n - \mathbf{u}_{ALE}^{n+1}) \cdot \nabla \mathbf{u}^{n+1} \\ -\nabla \cdot (2(\mu_{sgs}(\mathbf{u}^n) + \mu)\mathbf{D}(\mathbf{u}^{n+1})) + \nabla p^{n+1} \\ + \sum_{i=a,m} \frac{R}{\varepsilon} (\mathbf{u}^{n+1} - \mathbf{u}_{\Gamma_i}^{n+1}) \delta_{\Gamma_i, \varepsilon_i} = \mathbf{0}^3 & \text{in } \Omega^{n+1}, \\ \nabla \cdot \mathbf{u}^{n+1} = 0 & \text{in } \Omega^{n+1}, \\ \mathbf{u}^{n+1} = \widehat{\mathbf{u}}_{h,MRI}^{n+1} & \text{on } \Sigma_w^{n+1}, \end{cases} \quad (2)$$

with suitable initial conditions in Ω^0 .

The convective term in the momentum equation is treated in a semi-implicit way. $\mathbf{D}(\mathbf{u}^{n+1})$ is the velocity strain rate tensor defined by $\mathbf{D}(\mathbf{v}) = (\nabla \mathbf{v} + (\nabla \mathbf{v})^T)/2$. μ_{sgs} is the sub-grid viscosity of the σ -model given by $\mu_{sgs} = \rho C \Delta^2 \sigma_3 (\sigma_1 - \sigma_2) (\sigma_2 - \sigma_3) / \sigma_1^2$, with $\sigma_1(\mathbf{x}) > \sigma_2(\mathbf{x}) > \sigma_3(\mathbf{x})$ the singular values of $\nabla \mathbf{u}^n$. Δ is the average mesh element size equal to 1.5 mm for scenario H and R1 and 1.9 mm for R2; C is a constant set to the value of 1.5 [44, 45]. Notice the explicit treatment of the LES non-linearity.

R is the resistance coefficient of the RIIS model, whereas ε is half of the leaflets thickness. For both the mitral and aortic valves, we set $R = 10^4 \text{ kg/m} \cdot \text{s}$ [8] and $\varepsilon = 0.75 \text{ mm}$. $\mathbf{u}_{\Gamma_i}^{n+1}$, $i = m, a$, is the prescribed leaflets velocity. This

³with the symbol $\widehat{}$ we refer to the ED reference configuration

³When Γ_i is a subscript, we omitted the temporal index $n + 1$ for sake of clarity

is zero for both the mitral valve, since in this work we considered only the systolic phase, and the aortic valve, since the opening/closure mechanism in the regurgitant cases R1 and R2 was modeled in an on/off modality, by considering the two geometric configurations (open/closed) of the aortic valve template. The opening phase (modeled for R1 and R2, see Sect. 3.4) was instantaneous and triggered by a positive pressure jump between the ventricle and the aorta, whereas the closure occurred when a negative flow rate developed at the aortic valve plane [40, 17].

Finally, we have that $\delta_{\Gamma_i, \varepsilon_i}$, $i = m, a$, is a smoothed Dirac delta function representing a layer, with thickness 2ε , around the surface of the valve [41, 8].

Regarding the boundary conditions for problem (2), we prescribed at the atrial outlet Σ_1 a constant pressure of 10 mmHg for scenario H and a time dependent pressure taken from [16] for the regurgitant scenarios R1 and R2 (Fig. 3, right). In addition, in scenarios R1 and R2, to avoid possible backflows instabilities, we imposed null tangential velocity [46]. At the aorta outlet Σ_2 we imposed a time dependent physiological aortic pressure taken from [16] for all the the scenarios (Fig. 3, right). Finally, a no-slip condition is imposed on Σ_w in (2), prescribing the wall velocity coming from imaging.

To solve numerically the equations (1) and (2), we considered first-order Finite Elements. Equation (2) was stabilized by means of a Streamline Upwind Petrov–Galerkin/Pressure-Stabilizing Petrov-Galerkin (SUPG/PSPG) scheme [47, 48]. We used the multiphysics high performance library *life^x* [49] (<https://lifex.gitlab.io/>) based on the deal.II core [50] and developed in the iHEART project (<https://iheart.polimi.it/>).

Hexahedral meshes were generated by using suitable algorithms developed in VMTK [32]. The average mesh element size was equal to 1.5 mm (1.9 mm) with a local refinement of 0.4 mm (0.35 mm) close to the mitral valve for H and R1 (R2). These values were chosen after a mesh convergence analysis performed on scenario H, which showed differences of the quantities of interest of at most 2% when the mesh was refined by a factor 10%. Regarding the time discretization parameter, we set $\Delta t = 2.5 \cdot 10^{-4} s$, a value chosen after a convergence analysis that showed that halving this value the quantities of interest did not change within a discrepancy of 2%.

4 Numerical results

We started our analysis by discussing the opening/closure of the aortic valve. As stressed in Sect. 3.4, for scenario H we could not simulate the isovolumic contraction, thus we started our simulation at the instant $t_o = 0$ s just after the opening of the aortic valve. Instead, for R1 and R2 we observed that the pressure of the left ventricle was lower than the aortic one for $t = 0$ s, due to mitral regurgitation, see Fig. 4A, top (ventricle and aortic pressures were calculated on slices showed in Fig. 4B, left). In particular, the opening of the aortic valve occurred at $t_o = 0.010$ s and at $t_o = 0.016$ s for R1 and R2,

respectively.

Fig. 4A, top, also showed slightly larger values of the ventricle pressure for H with respect to R1 and R2, that featured very similar behaviors. This was also confirmed by the values reported in Table 1 where we computed the average in time (from t_o to the closure instant t_c) of the pressure drop $\overline{\Delta P}$ between the two slices of Fig. 4B, left.

Table 1: Values of the quantities of interest computed for the three scenarios. $\overline{\Delta P}$: pressure drop between ventricle and aorta; $t_c - t_o$: duration of the aortic ejection phase; SV : stroke volume; CO : cardiac output; RV : regurgitant volume; RF : regurgitant fraction; U_{AV} and U_{MV} : maximum velocity magnitude at the aortic valve and trough the mitral valve orifice; \bar{R} : average of the ratio between sub-grid and physical viscosity in the atrium; $\overline{WSS_{MV}}$ and $\overline{WSS_W}$: time average of the trend in time of the 1000 highest WSS magnitude on the mitral valve and on the walls.

Scenario	$\overline{\Delta P}$ [mmHg]	$t_c - t_o$ [s]	SV [mL]	CO [L/min]	RV [mL]	RF [%]	U_{AV} [m/s]	U_{MV} [m/s]	\bar{R} [-]	$\overline{WSS_{MV}}$ [Pa]	$\overline{WSS_W}$ [Pa]
H	5.5	0.32	92	6.9	0	0	1.8	0.0	0.1	0.4	0.8
R1	2.6	0.22	50	4.5	40	44	1.3	6.5	2.4	8.9	3.0
R2	2.0	0.26	85	6.4	89	51	0.9	5.3	3.2	6.2	2.7

The closing stage of the aortic valve in H occurred at $t_c = 0.32$ s, while in R1 and R2 much earlier, i.e. at $t_c = 0.24$ s and at $t_c = 0.28$ s, respectively. In Table 1, we reported the difference between t_c and t_o , representing the effective duration of the aortic ejection phase.

In Figure 4A, middle, we reported the trend in time of the flow rate evaluated at the level of the LVOT (Fig. 4B, middle). For all the three curves, we could recognize two significant peaks, at t_{v1} (yellow points) and at t_{v2} (black points) and a final phase of deceleration.

In Figure 4A, bottom, we reported the trend in time of the flow rate evaluated at the level of the mitral valve orifice (Fig. 4B, right). For R1 and R2, at t_o we had a local maximum due to the sudden opening of the aortic valve. After, both the curves started again to increase, reaching the global maximum at t_a (blue points) that was higher for R2.

From these curves we calculated some cardiac indices reported in Table 1: the stroke volume (SV) and the regurgitant volume (RV), obtained by integrating in time the flow rates evaluated at the level of the LVOT and through the mitral orifice, respectively; the cardiac output (CO), given by the product between SV and the heart rate and the regurgitant fraction (RF) defined as the ratio between RV and the sum of the SV and RV .

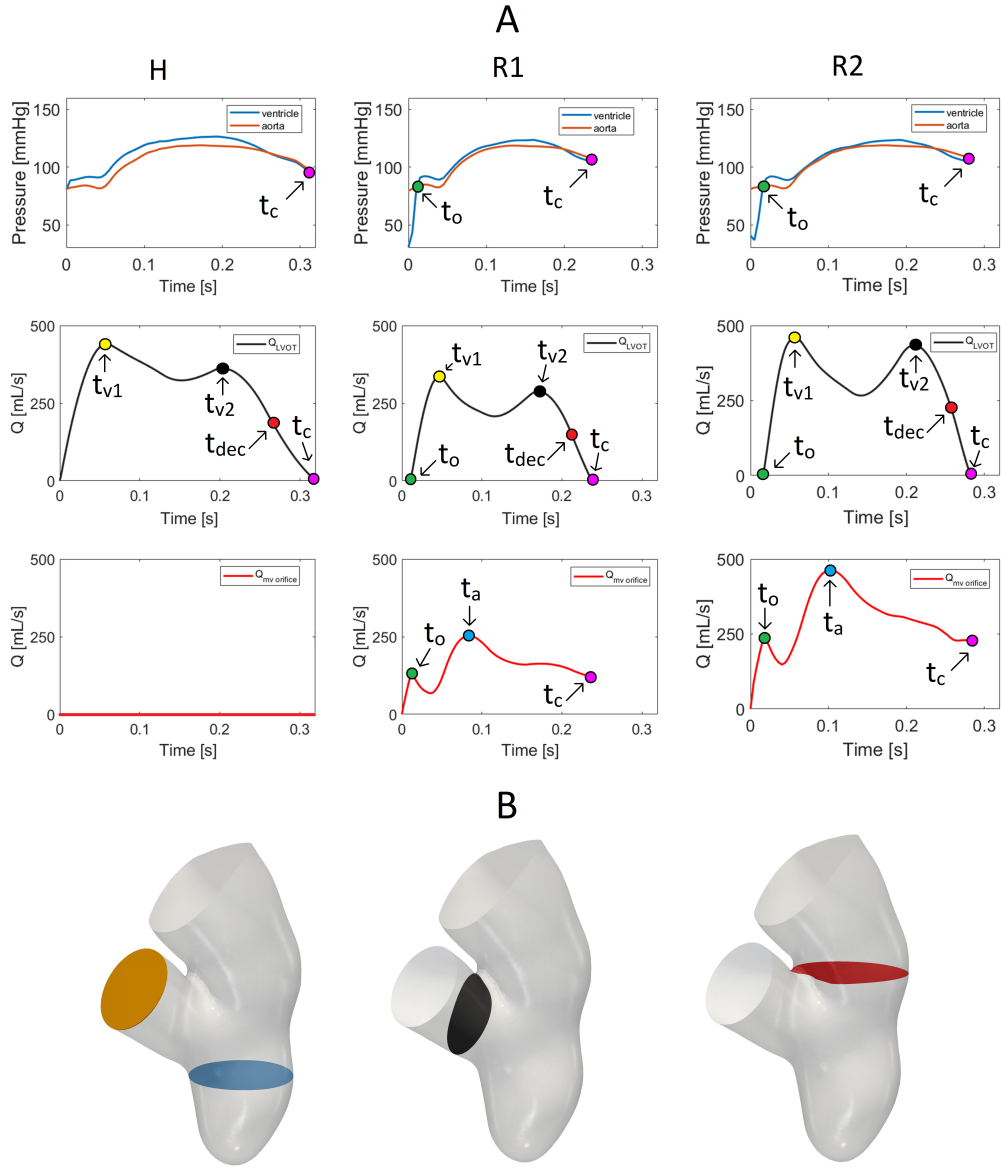


Figure 4: Panel A, top: trend in time of the ventricle and aortic pressures (computed in the blue and orange slices reported in panel B, left); t_o is the time instant where the aortic valve opens; t_c is the time instant where the aortic valve closes. Panel A, middle: plot over the time of the flow rate at the level of the LVOT (computed in the black slice reported in panel B, middle); t_{v1} and t_{v2} are the peak instants and t_{dec} the instant of middle deceleration. Panel A, bottom: plot over the time of the flow rate at the level of the mitral valve orifice (computed in the red slice reported in panel B, right); t_a is the time instant of the maximum flow rate. Panel B: sections of interest.

In Figure 5, the blood velocity field was represented on a 2D longitudinal slice to show the hemodynamics in the three scenarios. In particular, we considered

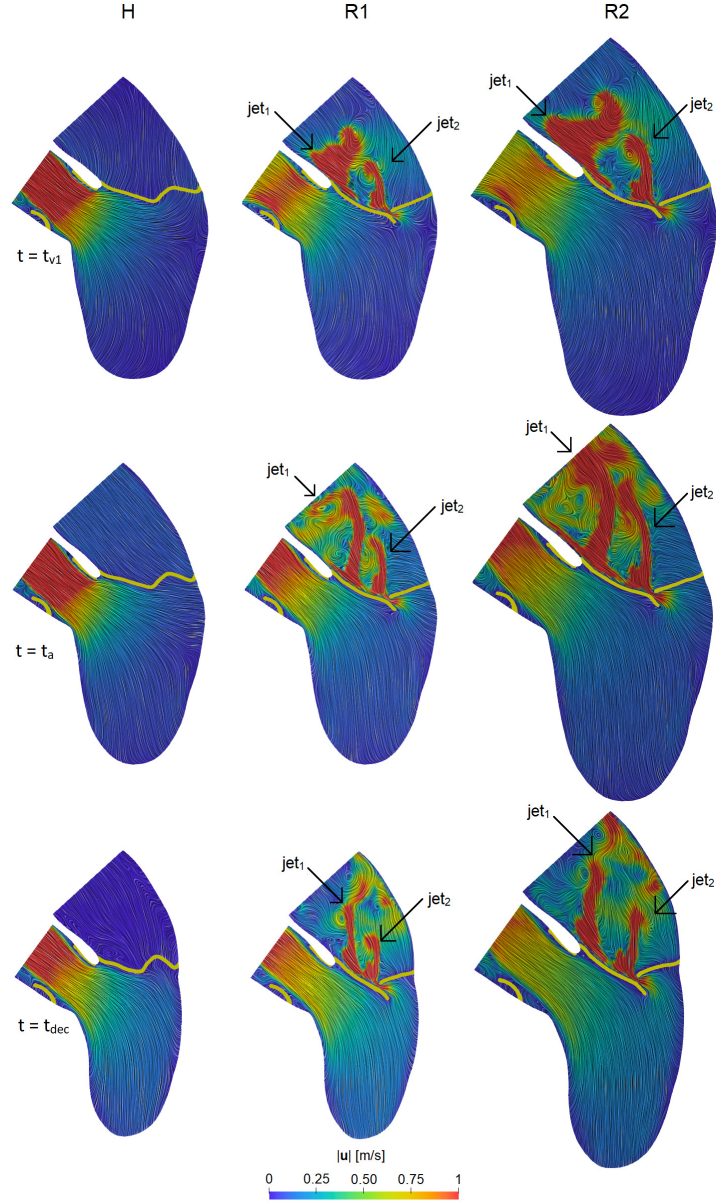


Figure 5: Velocity magnitude at three time instants in the three scenarios. In yellow we reported a slice of the two valves. For the instants refer to Fig 4A. For H we used the value of t_a taken from R2.

three representative time instants: t_{v1} , t_a (t_a for H being the same as R2) and the instant of middle deceleration of the ventricle flow rate, $t_{dec} = \frac{t_{v2} + t_c}{2}$, see Fig. 4A. We observed that, as expected, in scenario H all the blood flowed in the

aorta; instead, we noticed the formation of a *regurgitant jet* in the atrium for R1 and R2. At t_{v1} , in both the regurgitant cases the global velocity pattern was similar; the jet split in two different structures: one developing along the anterior leaflet (jet_1) and the other one arising directly from the free margin (jet_2) with a straighter direction. At t_a , also jet_1 assumed a straight configuration; in particular, in R2 the two jets collided close to the atrium outlet. In both R1 and R2 we also noticed that the velocities were elevated close to the wall of the atrium and that backflows formed at the outlet. At t_{dec} , the two jets split up in both the scenarios and, in correspondence of the atrial outlet, we noticed some fluctuations of the jets. In Table 1, we reported the maximum velocity magnitude U_{AV} and U_{MV} at the aortic valve plane and through the mitral valve orifice, respectively.

In Figure 6, top, the ratio μ_{sgs}/μ between turbulent and physical viscosity was reported in the three cases at t_a . From these results, we found elevated values of μ_{sgs} for R1 and R2 in the atrium, in particular in the regions with high velocities (see Fig. 5): at the level of the mitral valve orifice, where the sub-grid viscosity reached values also eight times greater than the value of the physical viscosity, and in the middle of the atrium, where chaotic and irregular velocity patterns were noticed (Fig. 5). Similar patterns were found for the other time instants. Instead, as expected, scenario H did not feature transition to turbulence. In Figure 6, bottom, we reported the trend in time of the average in the atrium of the ratio μ_{sgs}/μ for the regurgitant scenarios. In R2 we noticed a higher formation of turbulent viscosity as confirmed by Table 1, where we reported the average in time \bar{R} of μ_{sgs}/μ , confirming the essential absence of transition to turbulence in the H case.

In Figure 7, top, we reported the streamlines through the mitral and aortic orifices and the magnitude of the Wall Shear Stresses (WSS) on the mitral valve at instant t_a , for the regurgitant scenarios on three different views, namely *A*, *B* and *C*. We noticed a hotspot of shear forces localized at the mitral orifice, where high velocities occurred (see also Fig. 5). We also observed, as expected, a chaotic regurgitant flow downstream the valve orifice, with swirling structures filling the atrium. Although the velocity patterns were very similar, these chaotic structures were more evident in R2 due to the higher values of the flow rate. In particular, we noticed the presence of the two regurgitant jets jet_1 (developing along the anterior leaflet, view *B*) and jet_2 (impinging against the atrial walls, view *C*). In Figure 7, bottom, left, we reported a histogram showing the 1000 highest values of the WSS magnitude at t_a , clustered in four intervals. From this graph, we observed that most of the values fell in the range of $3 - 5 Pa$. In Figure 7, bottom, right, we computed the average of these points and plotted the trend in time. We noticed that R1 featured higher values than those for R2. This was also confirmed by the values reported in Table 1, where we computed the corresponding average in time \overline{WSS}_{MV} .

In Figure 8, top, we reported the volume rendering of the velocity magnitude and the spatial distribution of the WSS magnitude at instant t_a , evaluated in the

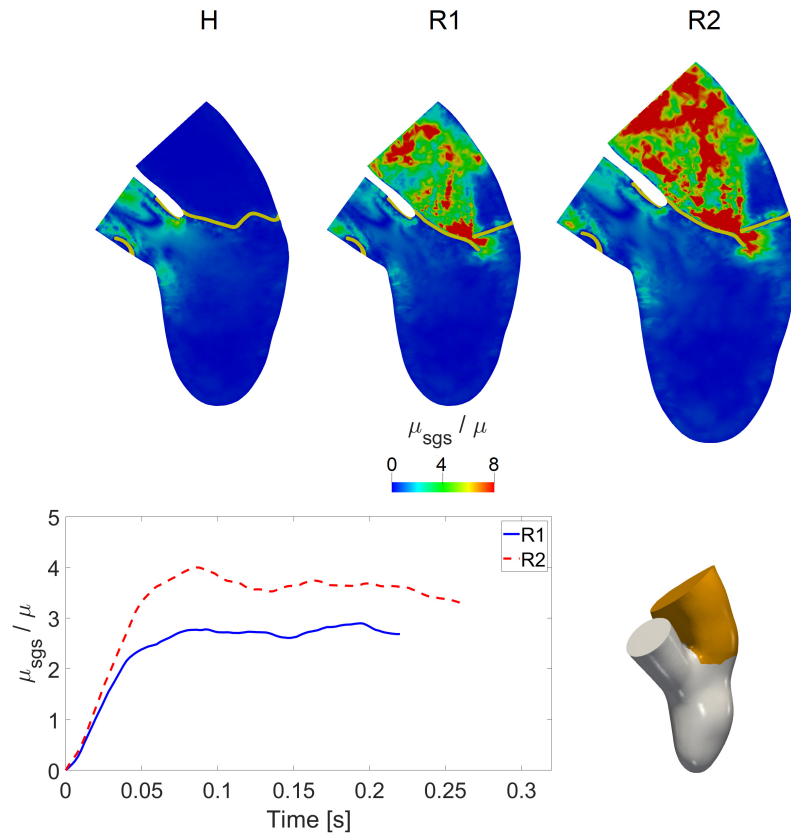


Figure 6: Top: ratio between the turbulent viscosity μ_{sgs} and the physical viscosity μ in the three scenarios at t_a . For H we used the value of t_a taken from R2. Bottom: trend in time of average in the atrium of the ratio between the turbulent viscosity μ_{sgs} and the physical viscosity μ for the regurgitant scenarios R1 and R2.

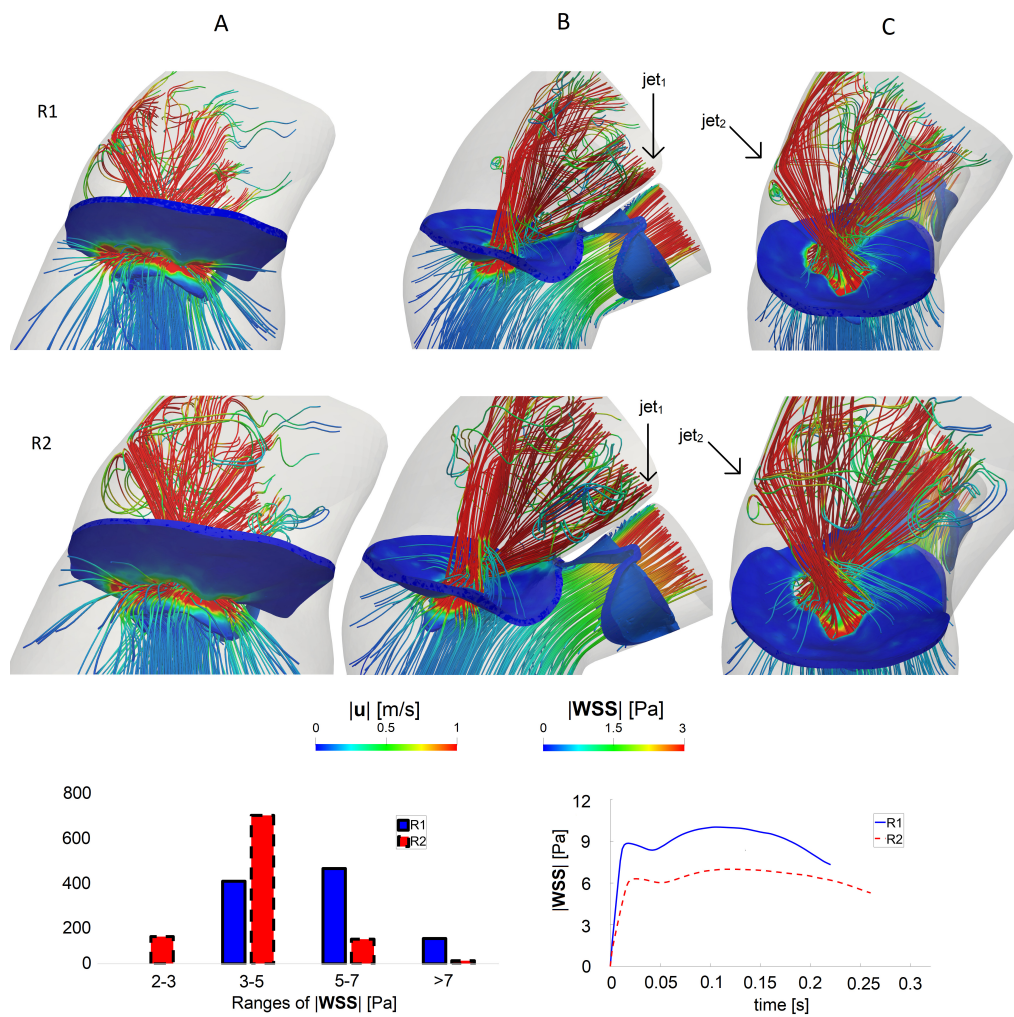


Figure 7: Top: streamlines of the velocity magnitude through the mitral and aortic orifice in R1 and R2 and magnitude of the WSS on the mitral valve at instant t_a in three different views. Bottom, left: distribution of the 1000 highest values of WSS magnitude on the mitral valve at t_a . Bottom, right: trend in time of the average of the 1000 highest values of the WSS magnitude.

atrial region for the regurgitant scenarios on two different perspectives. From this

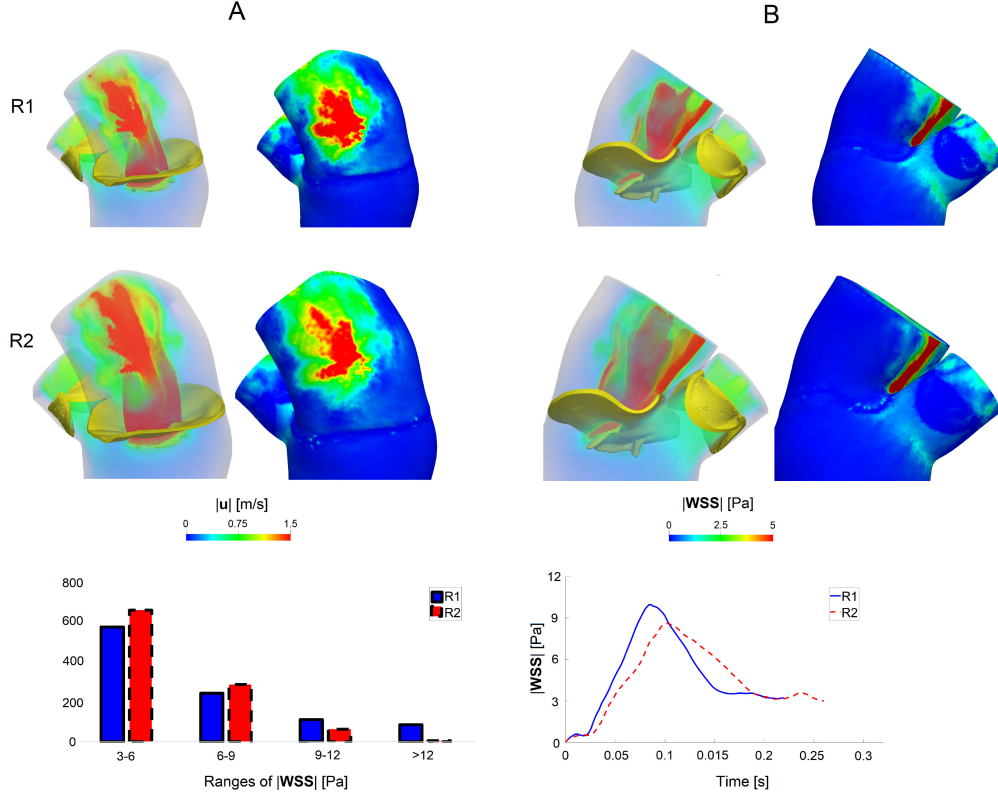


Figure 8: Top: for each of the columns A and B ($R1$ and $R2$, time t_a): Left, volume rendering of the velocity magnitude. Right: spatial distribution of the WSS magnitude. Bottom, left: distribution of the 1000 highest values of WSS magnitude in the wall of the atrium for $R1$ and $R2$ at t_a . Bottom, right: trend in time of the average of the 1000 highest values of the WSS magnitude in $R1$ and $R2$.

figure we observed that in $R1$ and $R2$ the combined action of the two regurgitant jets jet_1 and jet_2 gave rise to two different zones of high WSS: the area where the flow impinged against the wall of the atrium (view A) and the area where jet_1 rubbed against the wall of the atrium adjacent to the anterior leaflet (view B, refer also to Figs. 5 and 7). In Figure 8, bottom, left, we showed a histogram with the 1000 highest values of the WSS magnitude at t_a , clustered in four intervals. From this graph, we noticed that, although most of the values fell in the range 3 – 6 Pa, more elevated values of the WSS (up to 12 Pa, or even more for $R1$) were found for a significant number of points. In Figure 8, bottom, right, we computed the average of these points and we plotted their trend in time. We observed that the WSS highest values for $R1$ were in average slightly higher than those for $R2$, as confirmed by Table 1 where we reported the corresponding

average in time $\overline{WSS_W}$.

5 Discussion

In this work we performed an image-based computational study to analyze the hemodynamics in presence of a healthy (H) and regurgitant valve with either increased heart rate (R1) or dilated left ventricle (R2). These two phases represent two different mechanisms the heart employs to compensate the decreasing of the cardiac output (CO) due to MVR. This process is known as *heart remodeling*, however what is still unclear in the literature is the interplay between all the factors involved (such as pressure, velocity, volumes and shear forces) [51]. In particular, we found that in R1 and R2 the ventricle was not able to provide the same ventricular pressure of the H case (Fig. 4A, top, and values of $\overline{\Delta P}$ in Table 1). The consequence was the shortening of the aortic ejection phase interval $t_c - t_o$, with a delay of the opening of the aortic valve at t_o and an advance of the closing time t_c (see Table 1). This could be of interest for a better knowledge of the pathology, and also useful from the clinical point of view, since it may help the physician in the quantification of the degree of MVR.

In scenario H all the blood was ejected into the aorta with a flow peak at t_{v1} of 440 mL/s and a maximum ventricle pressure of 126.5 mmHg ; these values were consistent with standard physiological data [52, 53]. Instead, in R1 and R2 part of the blood flowed back to the atrium. In all the scenarios, the ventricular flow rate featured two peaks (Fig. 4A, middle). This specific behavior was previously found in other studies [54, 16, 55].

From the flow rates through the aortic and mitral valve we calculated some cardiac indices (see Table 1), used by the physicians to elaborate the diagnosis. In R1 and R2 we noticed that such indices fell into the physiological ranges [56] despite the reduced CO with respect to H, highlighting the ability of the system to compensate for MVR by increasing the heart rate and/or augmenting the ventricular dimensions. In particular, in R1 the increasing of the heart rate provided more blood flow to aorta than to left atrium (regurgitant fraction $RF < 50\%$). Instead, in R2 the ventricle dilation allowed to sustain a physiological value of SV , even if the volume of blood returning to the left atrium was larger ($RF > 50\%$).

Regarding velocity, in H the maximum velocity magnitude U_{AV} through the aortic valve was 1.8 m/s , a value comparable with those found in other studies [57, 58]. Instead in R1 and R2 we found chaotic velocity patterns in the atrium (Fig. 7) with values of 6.5 m/s and 5.3 m/s for the regurgitant velocity U_{MV} , respectively. These values were comparable with others found in literature [59, 60, 61]. Furthermore, in both cases, the regurgitant jet split in two different structures (Figs. 5, 7 and 8), one of which (jet_1) developed along the anterior leaflet. This behavior was in accordance with the Carpentier's functional classification [62, 63] where in case of MVR due to prolapse the jet is directed

away from the pathological leaflet, which in our case was the posterior one.

The formation of the regurgitant jet in the atrium led to high values of the subgrid viscosity of the turbulence model (Fig. 6 and turbulence index \bar{R} in Table 1) suggesting, for the first time, that the formation of turbulence in the left atrium could occur during the systole in the regurgitant cases, especially in the dilated scenario.

MVR also yielded to high values of WSS on the mitral valve and on the atrial wall (see Figs. 7, 8 and Table 1). It is well established in the literature that the WSS influence the cardiovascular development and remodeling [64] and our results highlighted that both in R1 and R2 the combined action of the two jets gave rise to high values of the shear forces in the left atrium (Fig. 8 and the values of \overline{WSS}_W in Table 1). This suggested that in MVR due to leaflet prolapse the left atrial size should be monitored by investigational tests, in order to prevent the risk of an excessive dilation of the wall leading potentially to atrial fibrillation [65, 66, 67], the most common complication of the MVR, or in more rare cases to aneurysm formation [68, 69].

In the regurgitant cases we also noticed elevated values of WSS on the mitral valve leaflets, in correspondence of the level of the free margins (Fig. 7 and the values of \overline{WSS}_{MV} in Table 1). While the action of the WSS on the vascular tissue is quite understood, their effects on the valvular tissue are still under debate [70]. A shared conjecture is that the repeated action of the shear forces at every cardiac cycle could damage the endothelial valve tissue and trigger numerous active mechanisms resulting in potential valve degeneration and calcification, worsening the degree of MVR [70].

6 Final Remarks and Limitations

The main outcomes and novelties of the present study could be summarized as follows:

1. We showed how it is possible to build a framework to obtain virtual scenarios in the moving ventricle to analyze systolic hemodynamics, without the need of using a fluid-structure interaction model and by using instead dedicated dynamic images of the left ventricle and of the mitral valve;
2. For the first time, we showed and quantified the presence of transition to turbulence in the atrium during systole in the regurgitant cases;
3. We compared two possible regurgitant scenarios providing a quantitative comparison of different hemodynamic quantities, highlighting the ability of the system to compensate MVR and recover a physiological cardiac output (albeit slightly smaller than the healthy case);
4. We quantified the chaotic velocity pattern in the atrium in the regurgitant cases highlighting the presence of two distinct jets; moreover, we assessed

the WSS magnitude on the mitral valve and atrium wall, focusing on the increase of viscous forces due to regurgitation.

Some limitations characterized this study:

1. Starting from a ventricular geometry segmented from MRI, we filled the missing geometric data, by considering a template for left atrium and aortic valve, and a flow extension for aorta. We are currently investigating the possibility to analyze more accurate MRI images including also aorta and left atrium;
2. We expanded harmonically the ventricular displacement to the wall of the left atrium and aorta. With this choice we neglected the dilation of the left atrium and aorta during the ventricular systole. This point is currently under scrutiny, to understand how to include plausible dilation motions of aorta and left atrium, following e.g. the strategy proposed in [71].
3. We simulated only the systole including the isovolumic contraction for R1 and R2, since MVR is a pathology affecting mostly the systole. However, it will be of scientific interest to complete this study by including also the diastolic phase encompassing the mitral leaflets opening.
4. We are aware that, in the clinical setting, the degree of mitral valve regurgitation, for the same type of valvular disease, is extremely variable, depending upon several variable factors, such as heart rate, ventricular contractility, pre-load and after-load. Our current study was limited to the description of hemodynamics considering only one degree of MVR and two possible scenarios (increased heart rate and increased ventricular dimensions), maintaining all other parameters unchanged in all groups.

7 Acknowledgments

The authors would like to thank the *iHEART* team for the technical support on *life^x*. AQ and CV are partially supported by the Italian project MIUR PRIN17 2017AXL54F “Modeling the heart across the scales: from cardiac cells to the whole organ”.

References

- [1] Harb, S.L., Griffin, B.P.: Mitral valve disease: a comprehensive review. *Curr Cardiol Rep.* **19**(73) (2017). <https://doi.org/10.1007/s11886-017-0883-5>
- [2] Wu, S., Chai, A., Arimie, S., Mehra, A., Clavijo, L., Matthews, R., Shavelle, D.: Incidence and treatment of severe primary mitral regurgitation in contemporary clinical practice. *Cardiovascular Revascularization Medicine* **19** (2018). <https://doi.org/10.1016/j.carrev.2018.07.021>

- [3] Kon, M., Myerson, S., Moat, N., Pennell, D.: Quantification of regurgitant fraction in mitral regurgitation by cardiovascular magnetic resonance: Comparison of techniques. *The Journal of heart valve disease* **13**, 600–7 (2004)
- [4] Falk, V., Seeburger, J., Czesla, M., Borger, M.A., Willige, J., Kuntze, T., Doll, N., Borger, F., Perrier, P., Mohr, F.W.: How does the use of polytetrafluoroethylene neochordae for posterior mitral valve prolapse (loop technique) compare with leaflet resection? A prospective randomized trial. *The Journal of Thoracic and Cardiovascular Surgery* **1200-1206**, 600–7 (2008). <https://doi.org/10.1016/j.jtcvs.2008.07.028>
- [5] Pfanmüller, B., Misfeld, M., Verevkin, A., Garbade, J., Holzhey, D.M., Davierwala, P., Seeburger, J., Noack, T., Borger, M.A.: Loop neochord versus leaflet resection techniques for minimally invasive mitral valve repair: long-term results. *European Journal of Cardio-Thoracic Surgery* **59**(1), 180–186 (2020)
- [6] Mittal, R., Seo, J.H., Vedula, V., Choi, Y., Liu, H., Huang, H., Jain, S., Younes, L., Abraham, T., George, R.: Computational modeling of cardiac hemodynamics: Current status and future outlook. *Journal of Computational Physics* **305** (2015). <https://doi.org/10.1016/j.jcp.2015.11.022>
- [7] Gao, H., Qi, N., Feng, L., Ma, X., Danton, M., Berry, C., Luo, X.: Modelling mitral valvular dynamics - current trend and future directions: Review of mv modelling. *International Journal for Numerical Methods in Biomedical Engineering* **33** (2016). <https://doi.org/10.1002/cnm.2858>
- [8] Fumagalli, I., Fedele, M., Vergara, C., Dede', L., Ippolito, S., Nicolò, F., Antona, C., Scrofani, R., Quarteroni, A.: An image-based computational hemodynamics study of the systolic anterior motion of the mitral valve. *Computers in Biology and Medicine* **123**, 103922 (2020). <https://doi.org/10.1016/j.compbiomed.2020.103922>
- [9] Kunzelman, K.S., Einstein, D.R., Cochran, R.P.: Fluid structure interaction models of the mitral valve: function in normal and pathological states. *Philosophical Transactions of the Royal Society B: Biological Sciences* **362**(1484), 1393–1406 (2007). <https://doi.org/10.1098/rstb.2007.2123>
- [10] Ma, X., Gao, H., Griffith, B., Berry, C., Luo, X.: Image-based fluid-structure interaction model of the human mitral valve. *Computers and Fluids* **71**, 417–425 (2013). <https://doi.org/10.1016/j.compfluid.2012.10.025>
- [11] Su, B., Zhong, L., Wang, X.-K., Zhang, J.-M., Tan, R.S., Allen, J.C., Tan, S.K., Kim, S., Leo, H.L.: Numerical simulation of patient-specific left ventricular model with both mitral and aortic valves by FSI approach.

- Computer Methods and Programs in Biomedicine **113**(2), 474–482 (2014). <https://doi.org/10.1016/j.cmpb.2013.11.009>
- [12] Gao, H., Feng, L., Qi, N., Berry, C., Griffith, B.E., Luo, X.: A coupled mitral valve-left ventricle model with fluid–structure interaction. *Medical Engineering Physics* **47**, 128–136 (2017). <https://doi.org/10.1016/j.medengphy.2017.06.042>
- [13] Feng, L., Gao, H., Griffith, B., Niederer, S., Luo, X.: Analysis of a coupled fluid-structure interaction model of the left atrium and mitral valve. *International Journal for Numerical Methods in Biomedical Engineering* **35**(11) (2019). <https://doi.org/10.1002/cnm.3254>
- [14] Caballero, A., Mao, W., McKay, R., Sun, W.: Transapical mitral valve repair with neochordae implantation: FSI analysis of neochordae number and complexity of leaflet prolapse. *International Journal for Numerical Methods in Biomedical Engineering* **36**(3), 3297 (2020). <https://doi.org/10.1002/cnm.3297>
- [15] Lassila, T., Malossi, A.C.I., Stevanella, M., Votta, E., Redaelli, A., Deparis, S.: Simulation of left ventricle fluid dynamics with mitral regurgitation from magnetic resonance images with fictitious elastic structure regularization (2017)
- [16] Caballero, A., Mao, W., McKay, R., Primiano, C., Hashim, S., Sun, W.: New insights into mitral heart valve prolapse after chordae rupture through fluid–structure interaction computational modeling. *Scientific Reports* **8** (2018). <https://doi.org/10.1038/s41598-018-35555-5>
- [17] Bavo, A., Pouch, A., Degroote, J., Vierendeels, J., Gorman III, J., Gorman, R., Segers, P.: Patient-specific CFD simulation of intraventricular haemodynamics based on 3D ultrasound imaging. *Biomedical engineering online* **15** (2016). <https://doi.org/10.1186/s12938-016-0231-9>
- [18] Bavo, A., Pouch, A., Degroote, J., Vierendeels, J., Gorman III, J., Gorman, R., Segers, P.: Patient-specific CFD models for intraventricular flow analysis from 3D ultrasound imaging: Comparison of three clinical cases. *Journal of Biomechanics* **50** (2016). <https://doi.org/10.1016/j.jbiomech.2016.11.039>
- [19] Vellguth, K., Brüning, J., Goubergrits, L., Tautz, L., Hennemuth, A., Kertzsch, U., Degener, F., Kelm, M., Sündermann, S., Kuehne, T.: Development of a modeling pipeline for the prediction of hemodynamic outcome after virtual mitral valve repair using image-based CFD. *International Journal of Computer Assisted Radiology and Surgery* **13** (2018). <https://doi.org/10.1007/s11548-018-1821-8>

- [20] Morud, J.C., Skjetne, P., Urheim, S., Dahl, S.K.: The effect of chordae tendineae on systolic flow. *Computers in Biology and Medicine* **109**, 91–100 (2019). <https://doi.org/10.1016/j.combiomed.2019.04.020>
- [21] Su, B., Tan, R.S., Tan, J.L., Guo, K.W.Q., Zhang, J.M., Leng, S., Zhao, X., Allen, J.C., Zhong, L.: Cardiac MRI based numerical modeling of left ventricular fluid dynamics with mitral valve incorporated. *Journal of Biomechanics* **49**(7), 1199–1205 (2016). <https://doi.org/10.1016/j.jbiomech.2016.03.008>
- [22] Fumagalli, I., Vitullo, P., Vergara, C., Fedele, M., Corno, A.F., Ippolito, S., Scrofani, R., Quarteroni, A.: Image-based computational hemodynamics analysis of systolic obstruction in hypertrophic cardiomyopathy. *Frontiers in Physiology* **12** (2022). <https://doi.org/10.3389/fphys.2021.787082>
- [23] Collia, D., Zovatto, L., Pedrizzetti, G.: Analysis of mitral valve regurgitation by computational fluid dynamics. *APL Bioengineering* **3**(3), 036105 (2019). <https://doi.org/10.1063/1.5097245>
- [24] Stevanella, M., Maffessanti, F., Conti, C., Votta, E., Arnoldi, A., Lombardi, M., Parodi, O., Caiani, E., Redaelli, A.: Mitral valve patient-specific finite element modeling from cardiac MRI: Application to an annuloplasty procedure. *Cardiovascular Engineering and Technology* **2**, 66–76 (2011). <https://doi.org/10.1007/s13239-010-0032-4>
- [25] Gaasch, W.H., Meyer, T.E.: Left ventricular response to mitral regurgitation. *Circulation* **118**(22), 2298–2303 (2008). <https://doi.org/10.1161/CIRCULATIONAHA.107.755942>
- [26] Bach, D.S., Deeb, G.M., Bolling, S.F.: Accuracy of intraoperative transesophageal echocardiography for estimating the severity of functional mitral regurgitation. *The American journal of cardiology* **76**(7), 508–512 (1995). [https://doi.org/10.1016/s0002-9149\(99\)80140-4](https://doi.org/10.1016/s0002-9149(99)80140-4)
- [27] Koelling, T., Aaronson, K., Cody, R., Bach, D., Armstrong, W.: Prognostic significance of mitral regurgitation and tricuspid regurgitation in patients with left ventricular systolic dysfunction. *American heart journal* **144**, 524–9 (2002). <https://doi.org/10.1067/mhj.2002.123575>
- [28] Fetzner, A., Zelzer, S., Schroeder, T., Meinzer, H.-P., Nolden, M.: An interactive 3D segmentation for the Medical Imaging Interaction Toolkit (MITK). (2014). <https://doi.org/10.13140/2.1.4169.6326>
- [29] Wolf, I., Vetter, M., Wegner, I., Böttger, T., Nolden, M., Schöbinger, M., Hastenteufel, M., Kunert, T., Meinzer, H.-P.: The medical imaging interaction toolkit. *Medical Image Analysis* **9**(6), 594–604 (2005). <https://doi.org/10.1016/j.media.2005.04.005>. ITK

- [30] Nolden, M., Zelzer, S., Seitel, A., Nabers, D., Müller, M., Franz, A., Maleike, D., Fangerau, M., Baumhauer, M., Maier-Hein, L., Maier-Hein, K., Meinzer, H.-P., Wolf, I.: The medical imaging interaction toolkit: challenges and advances. *International journal of computer assisted radiology and surgery* **8** (2013). <https://doi.org/10.1007/s11548-013-0840-8>
- [31] Antiga, L., Piccinelli, M., Botti, L., Ene-Iordache, B., Remuzzi, A., Steinman, D.A.: An image-based modeling framework for patient-specific computational hemodynamics. *Medical & biological engineering & computing* **46**(11), 1097–1112 (2008). <https://doi.org/10.1007/s11517-008-0420-1>
- [32] Fedele, M., Quarteroni, A.: Polygonal surface processing and mesh generation tools for the numerical simulation of the cardiac function. *International Journal for Numerical Methods in Biomedical Engineering* **37** (2021). <https://doi.org/10.1002/cnm.3435>
- [33] Klein, S., Staring, M., Murphy, K., Viergever, M.A., Pluim, J.P.W.: Elastix: A toolbox for intensity-based medical image registration. *IEEE Transactions on Medical Imaging* **29**(1), 196–205 (2010). <https://doi.org/10.1109/TMI.2009.2035616>
- [34] Chandraratna, P.A., Aronow, W.S.: Mitral valve ring in normal vs dilated left ventricle. cross-sectional echocardiographic study. *Chest* **79**(2), 151–154 (1981). <https://doi.org/10.1378/chest.79.2.151>
- [35] Ballester, M., Jajoo, J., Rees, S., Rickardsm, A., Mcdonald, L.: The mechanism of mitral regurgitation in dilated left ventricle. *Clinical Cardiology* **6**(7), 333–338 (1983). <https://doi.org/10.1002/clc.4960060706>
- [36] Hirt, C.W., Amsden, A.A., Cook, J.L.: An arbitrary Lagrangian-Eulerian computing method for all flow speeds. *Journal of Computational Physics* **14**(3), 227–253 (1974). [https://doi.org/10.1016/0021-9991\(74\)90051-5](https://doi.org/10.1016/0021-9991(74)90051-5)
- [37] Donea, J., Giuliani, S., Halleux, J.P.: An arbitrary Lagrangian-Eulerian finite element method for transient dynamic fluid-structure interactions. *Computer Methods in Applied Mechanics and Engineering* **33**(1), 689–723 (1982). [https://doi.org/10.1016/0045-7825\(82\)90128-1](https://doi.org/10.1016/0045-7825(82)90128-1)
- [38] Stein, K., Tezduyar, T., Benney, R.: Mesh moving techniques for fluid-structure interactions with large displacements. *Journal of Applied Mechanics* **70**(1), 58–63 (2003). <https://doi.org/10.1115/1.1530635>
- [39] Fernández, Miguel A., Gerbeau, Jean-Frédéric, Martin, Vincent: Numerical simulation of blood flows through a porous interface. *ESAIM: M2AN* **42**(6), 961–990 (2008). <https://doi.org/10.1051/m2an:2008031>

- [40] Astorino, M., Hamers, J., Shadden, S.C., Gerbeau, J.-F.: A robust and efficient valve model based on resistive immersed surfaces. *International Journal for Numerical Methods in Biomedical Engineering* **28**(9), 937–959 (2012). <https://doi.org/10.1002/cnm.2474>
- [41] Fedele, M., Faggiano, E., Dede, L., Quarteroni, A.: A patient-specific aortic valve model based on moving resistive immersed implicit surfaces. *Biomechanics and modeling in mechanobiology* **16**, 1779–1803 (2017). <https://doi.org/10.1007/s10237-017-0919-1>
- [42] Nicoud, F., Toda, H., Cabrit, O., Bose, S., Lee, J.: Using singular values to build a subgrid-scale model for large eddy simulation. *Physics of Fluids - PHYS FLUIDS* **23** (2011). <https://doi.org/10.1063/1.3623274>
- [43] Lancellotti, R.M., Vergara, C., Valdetaro, L., Bose, S., Quarteroni, A.: Large eddy simulations for blood dynamics in realistic stenotic carotids. *International Journal for Numerical Methods in Biomedical Engineering* **33**(11), 2868. <https://doi.org/10.1002/cnm.2868>
- [44] Vergara, C., Le Van, D., Quadrio, M., Formaggia, L., Domanin, M.: Large eddy simulations of blood dynamics in abdominal aortic aneurysms. *Medical Engineering & Physics* **47**, 38–46 (2017). <https://doi.org/10.1016/j.medengphy.2017.06.030>
- [45] Stella, S., Vergara, C., Giovannacci, L., Quarteroni, A., Prouse, G.: Assessing the disturbed flow and the transition to turbulence in the arteriovenous fistula. *Journal of Biomechanical Engineering* **141**(10) (2019). <https://doi.org/10.1115/1.4043448>
- [46] Bertoglio, C., Caiazzo, A., Bazilevs, Y., Braack, M., Esmaily, M., Gravenmeier, V., L. Marsden, A., Pironneau, O., E. Vignon-Clementel, I., A. Wall, W.: Benchmark problems for numerical treatment of backflow at open boundaries. *International Journal for Numerical Methods in Biomedical Engineering* **34**(2), 2918 (2018). <https://doi.org/10.1002/cnm.2918>
- [47] Tezduyar, T., Sathe, S.: Stabilization parameters in SUPG and PSPG formulations. *Journal of Computational and Applied Mechanics* **4**, 71–88 (2003)
- [48] Forti, D., Dedè, L.: Semi-implicit BDF time discretization of the Navier–Stokes equations with VMS-LES modeling in a high performance computing framework. *Computers & Fluids* **117**, 168–182 (2015). <https://doi.org/10.1016/j.compfluid.2015.05.011>
- [49] Africa, P.C., Piersanti, R., Fedele, M., Dede, L., Quarteroni, A.: life^x - heart module: a high-performance simulator for the cardiac function. Package 1: Fiber generation. *arXiv* (2022). <https://doi.org/10.48550/ARXIV.2201.03303>

- [50] Arndt, D., Bangerth, W., Blais, B., Fehling, M., Gasmöller, R., Heister, T., Heltai, L., Köcher, U., Kronbichler, M., Maier, M., Munch, P., Pelteret, J.-P., Proell, S., Simon, K., Turcksin, B., Wells, D., Zhang, J.: The deal.ii library, version 9.3. *Journal of Numerical Mathematics* **29**(3), 171–186 (2021). <https://doi.org/10.1515/jnma-2021-0081>
- [51] McCutcheon, K., Manga, P.: Left ventricular remodelling in chronic primary mitral regurgitation: Implications for medical therapy. *Cardiovascular Journal of Africa* **29**, 51–65 (2018). <https://doi.org/10.5830/CVJA-2017-009>
- [52] Gulsin, G.S., Singh, A., McCann, G.P.: Cardiovascular magnetic resonance in the evaluation of heart valve disease. *BMC Med Imaging* **17** (2013). <https://doi.org/10.1186/s12880-017-0238-0>
- [53] Carey, R.M., Whelton, P.K.: Prevention, detection, evaluation, and management of high blood pressure in adults: Synopsis of the 2017 American College of Cardiology/American Heart Association Hypertension Guideline. *Annals of Internal Medicine* **168**(5), 351–358 (2018). <https://doi.org/10.7326/M17-3203>
- [54] Chen, W., Gao, H., Luo, X., Hill, N.: Study of cardiovascular function using a coupled left ventricle and systemic circulation model. *Journal of Biomechanics* **49** (2016). <https://doi.org/10.1016/j.jbiomech.2016.03.009>
- [55] Sun, W., Mao, W., Griffith, B.E.: Chapter 7 - Computer modeling and simulation of heart valve function and intervention. In: Kheradvar, A. (ed.) *Principles of Heart Valve Engineering*, pp. 177–211 (2019). <https://doi.org/10.1016/B978-0-12-814661-3.00007-1>
- [56] Rusinaru, D., Bohbot, F. Y. and Djelaili, Delpierre, Q., Altes, A., Serbout, S., Kubala, M., Maréchaux, S., Tribouilloy, C.: Normative reference values of cardiac output by pulsed-wave Doppler echocardiography in adults. *The American journal of cardiology* **140**, 128–133 (2021). <https://doi.org/10.1016/j.amjcard.2020.10.046>
- [57] Mao, W., Caballero, A., McKay, R., Primiano, C., Sun, W.: Fully-coupled fluid-structure interaction simulation of the aortic and mitral valves in a realistic 3D left ventricle model. *PLOS ONE* **12**(9), 1–21 (2017). <https://doi.org/10.1371/journal.pone.0184729>
- [58] Vinayagam, D., Patey, O., Thilaganathan, B., Khalil, A., Khalil, D.: Cardiac output assessment in pregnancy: comparison of two automated monitors with echocardiography. *Ultrasound in Obstetrics and Gynecology* **49**, 32–38 (2017)
- [59] Alharthi, M., Mookadam, F., Tajik, J.: Echocardiographic quantitation of mitral regurgitation. *Expert review of cardiovascular therapy* **6**, 1151–60 (2008). <https://doi.org/10.1586/14779072.6.8.1151>

- [60] Pierard, L., Carabello, B.: Ischaemic mitral regurgitation: Pathophysiology, outcomes and the conundrum of treatment. *European heart journal* **31**, 2996–3005 (2010). <https://doi.org/10.1093/eurheartj/ehq411>
- [61] Salustri, A., Almaghrabi, A.: Mitral valve disease: correlation between the most important echocardiographic parameters and haemodynamics. *E-Journal of Cardiology Practice* **16** (2018)
- [62] Carpentier, A.: Cardiac valve surgery—the “French correction”. *The Journal of Thoracic and Cardiovascular Surgery* **86**(3), 323–337 (1983). [https://doi.org/10.1016/S0022-5223\(19\)39144-5](https://doi.org/10.1016/S0022-5223(19)39144-5)
- [63] Filsoufi, F., Carpentier, A.: Principles of reconstructive surgery in degenerative mitral valve disease. *Seminars in thoracic and cardiovascular surgery* **19**, 103–110 (2007). <https://doi.org/10.1053/j.semtcvs.2007.04.003>
- [64] McCormick, M., Manduchi, E., Witschey, W., Gorman, R., Gorman III, J., Jiang, Y.-Z., Jr, C., Barker, A., Yoon, S., Markl, M., Davies, P.: Spatial phenotyping of the endocardial endothelium as a function of intracardiac hemodynamic shear stress. *Journal of Biomechanics* **50** (2016). <https://doi.org/10.1016/j.jbiomech.2016.11.018>
- [65] Janse, M.J.: Why does atrial fibrillation occur? *European Heart Journal* **18**, 12–18 (1997). https://doi.org/10.1093/eurheartj/18.suppl_C.12
- [66] Vasan, R.S., Larson, M.G., Levy, D., Evans, J.C., Benjamin, E.J.: Distribution and categorization of echocardiographic measurements in relation to reference limits. *Circulation* **96**(6), 1863–1873 (1997). <https://doi.org/10.1161/01.CIR.96.6.1863>
- [67] Borger, M.A., Mansour, M.C., Levine, R.A.: Atrial fibrillation and mitral valve prolapse. *Journal of the American College of Cardiology* **73**(3), 275–277 (2019). <https://doi.org/10.1016/j.jacc.2018.11.018>
- [68] Mügge, A., Daniel, W.G., Angermann, C., Spes, C., Khandheria, B.K., Kronzon, I., Freedberg, R.S., Keren, A., Dennig, K., Engberding, R., Sutherland, G.R., Vered, Z., Erbel, R., Visser, C.A., Lindert, O., Hausmann, D., Wenzlaff, P.: Atrial septal aneurysm in adult patients. *Circulation* **91**(11), 2785–2792 (1995). <https://doi.org/10.1161/01.CIR.91.11.2785>
- [69] Dolan, J.M., Kolega, J., Meng, H.: High wall shear stress and spatial gradients in vascular pathology: A review. *Ann Biomed Eng* **5**, 1411–1427 (2013). <https://doi.org/10.1007/s10439-012-0695-0>
- [70] Hsu, C.-P.D., Hutcheson, J.D., Ramaswamy, S.: Oscillatory fluid-induced mechanobiology in heart valves with parallels to the vasculature. *Vascular Biology* **2**(1), 59–71 (2020). <https://doi.org/10.1530/VB-19-0031>

- [71] Zingaro, A., Fumagalli, I., Dede, L., Fedele, M., Africa, P.C., Corno, A.F., Quarteroni, A.: A geometric multiscale model for the numerical simulation of blood flow in the human left heart. *Discrete and Continuous Dynamical Systems - S*, (2022). <https://doi.org/10.3934/dcdss.2022052>

MOX Technical Reports, last issues

Dipartimento di Matematica
Politecnico di Milano, Via Bonardi 9 - 20133 Milano (Italy)

- 17/2022** Regazzoni, F.
Stabilization of staggered time discretization schemes for 0D-3D fluid-structure interaction problems
- 15/2022** G. Ciaramella, T. Vanzan
Spectral coarse spaces for the substructured parallel Schwarz method
- 16/2022** G. Ciaramella, T. Vanzan
Substructured Two-grid and Multi-grid Domain Decomposition Methods
- 14/2022** Zappon, E.; Manzoni, A.; Quarteroni A.
Efficient and certified solution of parametrized one-way coupled problems through DEIM-based data projection across non-conforming interfaces
- 13/2022** Grasselli, M.; Parolini, N.; Poiatti, A.; Verani, M.
Non-isothermal non-Newtonian fluids: the stationary case
- 12/2022** Antonietti, P.F.; Dassi, F.; Manzoni, E.
Machine Learning based refinement strategies for polyhedral grids with applications to Virtual Element and polyhedral Discontinuous Galerkin methods
- 11/2022** Sampaoli, S.; Agosti, A.; Pozzi, G.; Ciarletta, P.
A toy model of misfolded protein aggregation and neural damage propagation in neurodegenerative diseases
- 09/2022** Corti, M.; Zingaro, A.; Dede', L.; Quarteroni, A.
Impact of Atrial Fibrillation on Left Atrium Haemodynamics: A Computational Fluid Dynamics Study
- 10/2022** Fresca, S.; Manzoni, A.
Real-time simulation of parameter-dependent fluid flows through deep learning-based reduced order models
- 08/2022** Gobat, G.; Opreni, A.; Fresca, S.; Manzoni, A.; Frangi, A.
Reduced order modeling of nonlinear microstructures through Proper Orthogonal Decomposition